AIAA JOURNAL
Vol. 41, No. 3, March 2003

Effect of Geometrical Parameters on the Mixing Performance of Cantilevered Ramp Injectors

Bernard Parent* and Jean P. Sislian†
University of Toronto, Downsview, Ontario M3H 5T6, Canada

A cantilevered ramp fuel-injection strategy is considered as a means to deliver rapid mixing for use in scramjets and shock-induced combustion ramjets (shcramjets). The primary objective is to perform parametric studies of the injector array spacing, injection angle, and sweeping angle at a convective Mach number of 1.5. Analysis of the three-dimensional steady-state hypersonic flowfields is accomplished through the WARP code, using the Yee–Roe flux-limiting scheme and the Wilcox k-ω turbulence model, along with the Wilcox dilatational dissipation correction. A closer array spacing is shown to increase significantly the mixing efficiency in the near field, and a direct relationship between initial fuel/air contact surface and mixing efficiency growth is apparent. A change in the injector angle from 4 to 16 deg induces a 9% augmentation in the mixing efficiency but more than a twofold increase in the thrust potential losses. A sweeping angle of −3.5 deg is observed to result into significantly better fuel penetration, translating into a 28% increase in the mixing efficiency for a sweep angle decreased from 3.5 to −3.5 deg. It is observed that an air cushion between the wall and the hydrogen is sufficiently thick to prevent fuel penetrating the boundary layer when 1) the fuel is injected at an angle of ∼10 deg or more, 2) an array spacing of at least the height of the injector is used, and 3) a swept ramp configuration is avoided.

Nomenclature

A	=	area
a	=	speed of sound
c	=	mass fraction
F_{pot}	=	thrust potential
h	=	enthalpy
j	=	$(\gamma - 1)/\gamma$
k	=	turbulence kinetic energy
L_d	=	distance between injectors
L_f	=	length of incoming flat plate prior to injection
M	=	Mach number
M_c	=	convective Mach number, $(q_1 - q_2)/(a_1 + a_2)$
M_t	=	turbulent Mach number, $\sqrt{(2k)}/a$
$\dot{m}$	=	mass flow rate
P	=	pressure
$P^\star$	=	effective pressure, $P + \frac{2}{3}\rho k$
q	=	magnitude of the velocity vector
R	=	gas constant
T	=	temperature
u	=	velocity component along x
x, y, z	=	Cartesian coordinates
y^+	=	nondimensional wall distance, $(y/\mu)\sqrt{(\rho\tau_w)}$
γ	=	ratio of the specific heats
η_m	=	mixing efficiency
θ_c	=	injector compression angle
θ_e	=	injector expansion angle
μ	=	viscosity
ρ	=	density
τ_w	=	shear stress at the wall
$\Phi(P^\circ)$	=	thrust potential term function of P°
$\Phi(T^\circ)$	=	thrust potential term function of T°
ϕ	=	equivalence ratio
ψ	=	sweeping angle
ω	=	specific dissipation rate

Subscripts

a	=	engine inlet
b	=	station of interest
c	=	engine outlet

Superscripts

R	=	reacting
S	=	stoichiometric
$\star$	=	sum of the molecular and turbulent counterparts
$\circ$	=	stagnation

Introduction

SUPERSONIC combustion ramjets (scramjets) and shock-induced combustion ramjets[1] (shcramjets) differ from their ramjet counterpart by maintaining the flow supersonic throughout the engine. Although this is beneficial to the performance of the engine in the hypersonic range by avoiding the excessive losses associated with flow deceleration, a high flow speed necessarily induces a short residence time of the air particles flowing through the different components. Consequently, one challenging task associated with the design of supersonic combustion engines is the proper mixing of the fuel with the incoming air, a process that must be accomplished typically in under 1 ms.

Adding to the challenge is the well-known reduction in growth of the compressible turbulent mixing layer associated with a high convective Mach number.[2] This prevents a parallel mixing configuration relying purely on a high velocity difference between the air and the fuel from being competitive. Further, a very high convective Mach number induces appreciable total pressure losses.[3] A mixing strategy that is thought to be considerably better is through the use of ramp injectors, as first suggested by Marble et al.[4] and Waitz et al.[5] Ramp injectors are beneficial to the mixing performance by creating axial vortices, which increase the fuel penetration and the fuel/air contact surface. Nonetheless, ramp-injectors are also subject to reduced turbulence growth caused by compressibility effects, even at low convective Mach numbers,[6] because of the high local shear stresses induced by the streamwise vortices. A variant to the conventional ramp-injector model, named the cantilevered ramp

Received 25 March 2002; revision received 20 September 2002; accepted for publication 3 October 2002.

*Graduate Student, Department of Aerospace Engineering, Institute for Aerospace Studies; currently Postdoctoral Fellow, Department of Aerospace Engineering, Seoul National University, Seoul 151-744, Republic of Korea; bernard@snu.ac.kr. Student Member AIAA.

†Professor, Institute for Aerospace Studies, 4925 Dufferin Street; sislian@caius.utias.utoronto.ca. Associate Fellow AIAA.

injector, is shown by Sislian and Schumacher[7] and Parent and Sislian[8] to be superior to the ramp injector by preventing the fuel from being mixed with the hot incoming boundary layer and by generating stronger axial vortices.

To the authors' knowledge, no parametric study of the effect of array spacing, injection angle, and sweeping angle on the mixing performance of a ramp injector at a high convective Mach number has been reported. Previous work on array spacing includes the experimental investigation by Waitz et al.,[9] showing that at matched fuel/air velocities a reduction in the injector array spacing induces better mixing while exhibiting weaker axial vortices. The use of a swept configuration has been observed numerically and experimentally[10–13] to result in stronger axial vortices and better mixing. However, in all reported cases the convective Mach number is low, not exceeding 0.33. The primary objective of this paper hence is to assess the effect of array spacing, injection angle, and sweeping angle on the mixing efficiency, mass-flux-averaged stagnation pressure, and thrust potential of the cantilevered ramp injector at a convective Mach number of 1.5.

The results are obtained with the Window Allocatable Resolver for Propulsion (WARP) code outlined in Refs. 6 and 14, solving the Favre-averaged Navier–Stokes equations closed by the Wilcox k-ω turbulence model[15] and the Wilcox dilatational dissipation term[16] to account for compressibility effects occurring at high turbulent Mach number. The marching window acceleration technique[14] is used to obtain fast convergence to steady state. The injector problems studied herein are representative of fuel injection in the inlet of a shcramjet at a flight Mach number of 11.

Numerical Method

Governing Equations

The three-dimensional multispecies Favre-averaged Navier–Stokes equations closed by the Wilcox k-ω turbulence model[15] are solved to steady state. A thermally perfect gas is assumed, and polynomials[17] function of the temperature are used for the determination of the enthalpy and specific heat at constant pressure (valid in the range $200 < T < 6000$ K). The modeling of the dilatational dissipation correction term by Wilcox[16] is added to the turbulence kinetic energy transport equation to model the effect of reduced shear-layer growth at high convective Mach number, as first reported by Papamoschou and Roshko.[2] The addition of the dilatational dissipation model gives accurate shear-layer growths while not affecting the accuracy of the k-ω model in boundary layers, which has been verified up to a freestream Mach number of 6 (Ref. 6). This choice of turbulence model and compressibility correction has been validated[6] vs the experimental data of ramp injectors[5,12] with very good agreement on the basis of the injectant mass fraction contours. The experimental data of ramp injectors in the open literature are for moderate convective Mach number and moderate axial vortices strength, where the effect of the dilatational dissipation term is weak. However, the compressibility correction term is included in this model as it is shown to be necessary when tackling high-convective-Mach-number flowfields[16] but also when tackling this particular cantilevered ramp injector at matched fuel/air velocities.[6]

Discretization and Integration

The governing equations are written in strong conservation form and discretized using second-order accurate finite difference central stencils except for the convection derivative, which is discretized using the Yee–Roe[18,19] flux-limited method. The cantilevered injector flowfield can be tackled with the stand-alone Yee–Roe scheme without the need for an entropy correction term.[6] The use of the Yee entropy correction is detrimental to the accuracy of the discretization by increasing the amount of numerical diffusion in the shear layer and boundary layer and is hence avoided. The solution is iterated in pseudotime using a block-implicit approximate factorization algorithm and a linearization strategy of the viscous terms by Chang and Merkle.[20] The use of the marching window acceleration technique[14] results in a 10-fold decrease in computing time for the problems shown herein, and convergence to steady state is reached typically in 200–300 effective iterations, with a weak dependence on the grid dimensions. The same convergence criterion as shown in Ref. 6, which has been determined to be sufficient for a similar problem geometry and flow conditions to those used herein, is used. Structured meshes ranging from 1.5 to 3.2 million nodes are used, all with a similar mesh density to the grid used in Ref. 6, which is shown to result in a maximum of 7–22% relative error on the performance parameters of interest. The node spacing at all surfaces is set to 30 μ, which translates into a value for y^+ ranging between two and three in the mixing region. This has been observed[6] to be sufficiently small for an accurate representation of the wall shear stress and boundary-layer profiles in the injector domain.

Injector Configuration

Inflow Conditions

The inflow properties of the air and the fuel are the same for all configurations. Fuel injection is assumed to take place after the first shock in the inlet of an external compression shcramjet at a flight Mach number of 11. The shcramjet inlet is designed assuming a flight dynamic pressure of 67 kPa, two equal strength inlet shocks, a 900 K temperature prior to the detonation wave, and an inlet length of 0.7 m. This results in air properties of $P = 4758$ Pa, $T = 462$ K, and $M = 7.73$ after the first inlet shock, which are used as air inflow properties for the injection cases studied herein. The fuel is injected at a global equivalence ratio of 1, at a convective Mach number of 1.5, and at matched pressure with the air. This results in inflow properties for hydrogen of $P = 4758$ Pa, $T = 410$ K, and $M = 4.1$. The velocity difference between the hydrogen jet and the freestream is 2960 m/s. The hydrogen stagnation temperature is 1780 K, which is a desirable high value as the fuel is expected to cool the exposed surfaces of the engine and of the injector.

Problem Geometry

The present study assumes a slightly longer mixing region length of 1 m than the inlet length (set to 0.7 m) to account for the increase in mixing per unit length that is expected to occur because of the reduction in flow height by the shocks in the inlet. A schematic of the cantilevered ramp injector configuration used for all cases is shown in Fig. 1. A 1-cm-long fuel runway zone is specified inside the injector to avoid a singularity in the turbulence and flow properties at the point of injection. This alleviates the sensitivity of the k-ω model to the freestream value of ω (Ref. 6). The injection angle θ_c and sweep angle ψ are varied for the cantilevered injector. The cross-sectional area of the fuel per unit depth (along the z coordinate) is the same for all cases, a necessary condition for equal fuel inflow conditions and global equivalence ratio. In all cases the wall temperature is fixed to the air freestream temperature.

The cases in Table 1 have the following terminology: the first letter stands for a cantilevered ramp-injector configuration, which is followed by a number related to the convective Mach number of the system that is fixed for all cases to 1.5. The letter f refers to a case where the incoming air travels along a 50-cm flat plate before flowing around the injector, c to a case varying the injection angle, d to a case where the distance between injectors is varied, and e to

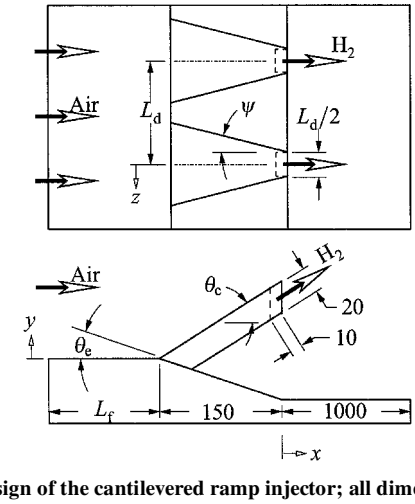

Fig. 1 Design of the cantilevered ramp injector; all dimensions are in millimeters unless otherwise noted.

Table 1 Test cases

Case	Mesh dimensions	L_d, m	L_f, m	θ_c, deg	θ_e, deg	ψ, deg
C5	$320 \times 187 \times 42$	0.04	0.0	10.0	6.0	0.0
C5f	$413 \times 187 \times 42$	0.04	0.5	10.0	6.0	0.0
C5c	$320 \times 187 \times 42$	0.04	0.0	16.0	0.0	0.0
C5c2	$320 \times 187 \times 42$	0.04	0.0	4.0	12.0	0.0
C5d1	$320 \times 187 \times 32$	0.0283	0.0	10.0	6.0	0.0
C5d2	$320 \times 187 \times 25$	0.02	0.0	10.0	6.0	0.0
C5d3	$320 \times 187 \times 54$	0.0566	0.0	10.0	6.0	0.0
C5d4	$320 \times 187 \times 25$	0.01	0.0	10.0	6.0	0.0
C5e	$320 \times 187 \times 42$	0.04	0.0	10.0	6.0	3.5
C5e2	$320 \times 187 \times 42$	0.04	0.0	10.0	6.0	−3.5

a case varying the sweeping angle. The turbulent Schmidt number is set to 1 for all cases.

Boundary Conditions

The schematic of the cantilevered ramp injector configuration shown in Fig. 1 assumes an infinite array of injectors along the z coordinate. This reduces the size of the computational domains by fixing symmetry planes at $z = L_d/2$ and 0. The top boundary (along the y coordinate) for all configurations is set to outflow, whereas the bottom boundary is a fixed temperature no-slip wall.

Performance Parameters

Mixing Efficiency

The mixing efficiency is here defined at station b (Fig. 2) as the ratio between the mass flow rate of oxygen that would burn and the mass flow rate of oxygen entering the computational domain:

$$\eta_m \equiv \frac{\int_b c^R_{O_2}\,\mathrm{d}\dot{m}}{\int_a c_{O_2}\,\mathrm{d}\dot{m}} \tag{1}$$

where the integral on the denominator corresponds to 1.363 kg/ms multiplied by the domain depth. The flow exiting the top boundary of the domain is taken into account. The fact that Eq. (1) assumes the fuel/air mixture to burn independently of the equivalence ratio leads to an overestimation of the mixing efficiency when the equivalence ratio does not lie within the flammability limits of hydrogen/air chemistry, that is, $0.1 < \phi < 7$ at atmospheric pressure. The reacting mass fraction of oxygen corresponds to

$$c^R_{O_2} = \begin{cases} c_{O_2} & \text{if} \quad c_{H_2} > c^S_{H_2} \\ c^S_{O_2} c_{H_2} \big/ c^S_{H_2} & \text{otherwise} \end{cases} \tag{2}$$

with the stoichiometric mass fraction of hydrogen $c^S_{H_2}$ equal to 0.02876 and the stoichiometric mass fraction of oxygen $c^S_{O_2}$ equal to 0.22824.

Averaged Stagnation Pressure

The mass-flux-averaged stagnation pressure can be expressed as

$$P^\circ_{\text{ave}} \equiv \frac{\int_b P^\circ\,\mathrm{d}\dot{m}}{\int_b \mathrm{d}\dot{m}} \tag{3}$$

where the stagnation pressure P° is defined as the pressure obtained when the flow is decelerated to stagnation on a reversible path. When defined in this manner, the stagnation pressure can be used as a measure of irreversible phenomena. The effect of turbulence is taken into account throughout the path to stagnation by freezing the turbulence kinetic energy, that is,

$$k = \text{constant} \tag{4}$$

For a noncalorically perfect gas it is not possible to obtain a closed-form solution for the stagnation pressure, and one must resort to a numerical integration of the momentum equation from the flow state $P^\star = P^\star_b$, $\rho = \rho_b$, $q = q_b$ to the stagnation state $P^\star = P^\circ$, $\rho = \rho^\circ$, $q = 0$:

$$\int_{P^\star_b}^{P^\circ} \mathrm{d}P^\star = \int_{q_b}^{0} -\rho q\,\mathrm{d}q \tag{5}$$

where ρ is updated after each small step from the thermally perfect gas equation of state

$$\rho = P^\star \big/ \left(RT + \tfrac{2}{3}k\right) \tag{6}$$

with the temperature T determined from the conservation of total enthalpy, which is solely a function of the temperature and the flow speed caused by the turbulence kinetic energy being constant along the integration path. Hence, the enthalpy can be expressed as

$$h = -q^2/2 + h_b + q_b^2/2 \tag{7}$$

from which T can be found directly. Then, Eq. (5) can be reformatted, assuming thermally perfect but not necessarily calorically perfect gas, to

$$P^\circ = P^\star_b \exp\left(\int_0^{q_b} \frac{q}{RT + \frac{2}{3}k}\,\mathrm{d}q \right) \tag{8}$$

which, in the special case of a calorically perfect gas, becomes the well-known algebraic expression for the compressible stagnation pressure provided the sound speed is taken as $[\frac{2}{3}\gamma k + (\gamma - 1)h]^{1/2}$, as specified in Ref. 14. For the governing equations tackled herein (which do not assume the gas to be calorically perfect), it is essential to determine the integral of Eq. (8) numerically, with the temperature found from the conservation of total enthalpy. The Simpson rule using 300 steps is found to give an accurate enough value for P°. Note that the turbulence kinetic energy k is constant along the path to stagnation, which follows from the omission of the source terms for the k and ω transport equations when integrating P°.

Thrust Potential

Because the mixing region is subject to significant total temperature variations, the mass-flux-averaged stagnation pressure is not indicative of the real losses incurred in the fuel/air mixing problem, and, therefore, cannot be directly related to the thrust of the engine. The thrust potential addresses this issue by measuring exactly how much thrust the engine would generate by taking the difference in momentum between the engine outlet and inlet, with the outlet found from a reversible expansion of the flow at the station where the thrust potential is to be evaluated. Referring to Fig. 2, the thrust potential is defined as[21]

$$\text{thrust potential} \equiv \left[\int_c (\rho u^2 + P^\star)\,\mathrm{d}A - \int_a (\rho u^2 + P^\star)\,\mathrm{d}A \right] \Big/ \dot{m} \tag{9}$$

where $\dot{m}$ can be taken as the mass flow rate of air through the engine, equal in this case to 5.91 kg/s for a domain depth of 1 m. For the engine configuration shown in Fig. 2, the thrust potential can be readily determined as the difference between the outlet momentum and the inlet momentum, minus the shear stresses on the top and bottom boundaries of the engine. The drag on the exterior of the

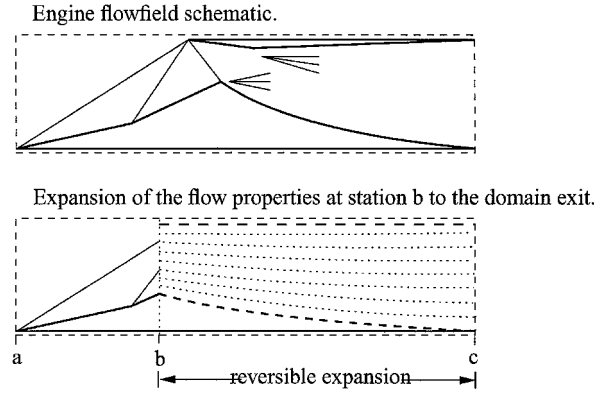

Fig. 2 Hypersonic engine schematic: top, control volume boundaries used to determine the thrust of the engine; bottom, control volume boundaries used to determine the thrust potential at station b, with the flow reversibly expanded from station b to station c.

engine is largely independent of the flowfield characteristics inside the engine and is ignored for the determination of the thrust potential. Further, Fig. 2 implies that the flow area at the outlet matches the one at the inlet. This is a reasonable assumption because scramjet flows are typically underexpanded[22] with a pressure at the exit greater than ambient, and the area cannot be made much larger than the inlet area to minimize the drag forces on the external surfaces. Therefore the definition of the thrust potential is based on a fixed outlet area, equal to the inlet area, with the pressure specified to be equal for all streamlines at the outlet, but not forced to a specific value. This is possible if the area increase ratio for each streamline is allowed to differ in such a way that all streamlines at station c exhibit the same pressure.

Implementation

The determination of the thrust potential at station b is performed iteratively. The first step consists of guessing a desired pressure at the exit $P_c^\star$ and in finding the velocity at station c reversibly expanded from each point at station b. The velocity at the exit is here referred to by q_c and is found by numerically differentiating

$$\frac{\mathrm{d}q}{\mathrm{d}P^\star} = -\frac{RT + \frac{2}{3}k}{P^\star q} \tag{10}$$

from q_b and $P_b^\star$ until $P_c^\star$ is reached. For the flow regions where the stagnation pressure [as calculated from Eq. (8)] is less than $P_c^\star$, the contribution to the thrust potential is ignored. The turbulence kinetic energy k is held constant throughout the differentiation, and the temperature can be expressed as a function of the magnitude of the velocity vector q from the conservation of total enthalpy. In the case of a calorically perfect gas, the latter can be integrated analytically, but for a high-temperature gas a numerical differentiation using the modified Euler algorithm[19] and 300 steps is used. Equation (10) yields T_c, ρ_c, and q_c for each streamline. Because the total area at station c is to match the area at the engine entrance, the problem is closed when

$$f\left(P_c^\star\right) = A_c\left(P_c^\star\right) - A_a = \int_b \frac{1}{\rho_c q_c}\,\mathrm{d}\dot{m} - A_a \tag{11}$$

is minimized, yielding $P_c^\star$. Then, each point at station b can be expanded a last time through Eq. (10) to the correct exit pressure, giving a thrust potential equal to

$$F_{\mathrm{pot}} = -F_{\mathrm{pot,ref}} + \int_b \frac{\rho_c q_c^2 + P_c^\star}{\rho_c q_c}\,\mathrm{d}\dot{m} \Big/ \dot{m}_{\mathrm{air,engine}} \tag{12}$$

For the shcramjet considered herein the area at the inlet and outlet A_a corresponds to $0.075 \times L_d$ m^2, whereas the reference thrust potential $F_{\mathrm{pot,\,ref}}$ is set to 3403 m/s. If the thrust potential is applied to a flowfield obtained using a numerical method that is *not* in control-volume form, it is necessary to multiply the second term on the right-hand side of Eq. (12) by the ratio between the exact mass flow and the numerical mass flow at station b, which typically differs very slightly from unity. This correction is performed to alleviate the dependence of the thrust potential to small (fictitious) variations in the mass flow rate present in a flowfield generated by a non-control-volume numerical method.

Alternate Formulation

Assuming a calorically perfect gas, and no turbulence, the thrust potential expressed in Eq. (12) can be shown to be equal to

$$F_{\mathrm{pot}} = -F_{\mathrm{pot,ref}} + \int_b \Phi(T^\circ)\Phi(P^\circ)\,\mathrm{d}\dot{m} \Big/ \dot{m}_{\mathrm{air,engine}} \tag{13}$$

where $\Phi(T^\circ)$ and $\Phi(P^\circ)$ correspond to

$$\Phi(T^\circ) = \left(\frac{2RT^\circ}{j}\right)^{\frac{1}{2}} \tag{14}$$

$$\Phi(P^\circ) = \frac{1 + (j/2 - 1)(P_c/P^\circ)^j}{\left[1 - (P_c/P^\circ)^j\right]^{\frac{1}{2}}} \tag{15}$$

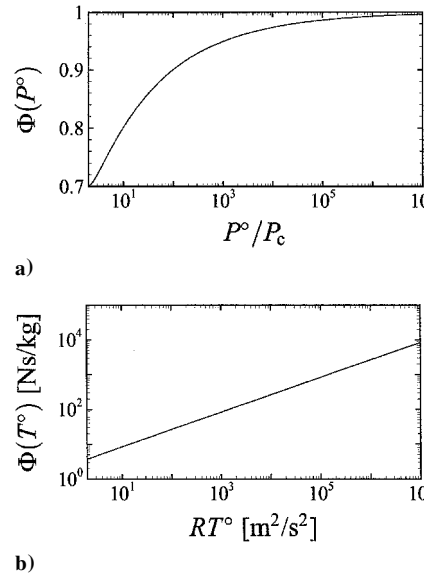

Fig. 3 Thrust potential terms $\Phi(T^\circ)$ and $\Phi(P^\circ)$, as defined in Eqs. (14) and (15) using $\gamma = 1.4$.

and with $j = (\gamma - 1)/\gamma$. In Eqs. (14) and (15) the stagnation pressure P° and temperature T° correspond to the well-known expressions for a calorically and thermally perfect gas with no turbulence. The function $\Phi(P^\circ)$ is plotted vs P°/P_c in Fig. 3a, and the influence of the latter on the thrust potential is seen not to be too severe, even when P°/P_c decreases 10-fold. The maximum fraction of the incoming momentum flux that can be taken away by a loss in stagnation pressure is seen to be ~30% for $\gamma = 1.4$. However, a cut of 30% of the incoming momentum can still be quite considerable, especially at high flight speeds. Further, it is seen to be very desirable to lower P_c, and hence raising the ratio P°/P_c where a change in the stagnation pressure has a lesser impact on the thrust potential. This is very important for hypersonic engines where several oblique shocks are present through which the flow experiences high changes in stagnation pressure but no change in stagnation temperature.

Figure 3b shows the relation between RT° and $\Phi(T^\circ)$, where a high dependence of the thrust potential on the stagnation temperature is observed, which is at the origin of the inadequacy of the mass-flux-averaged stagnation pressure in assessing losses. Furthermore, the importance of calculating the pressure at the exit P_c is made clearer, as the exit pressure is always coupled with the stagnation pressure in Eq. (15). Expanding the flow to ambient pressure, as opposed to finding the exit pressure iteratively, could lead to some quite large errors and would be just as erroneous as not evaluating the stagnation pressure correctly.

Results and Discussion

Injector Array Spacing

This subsection investigates a change in injector array spacing on the mixing performance of the cantilevered ramp injector. The injector depth (along the z coordinate) is varied proportionally to the array spacing, such that the global equivalence ratio and the inlet conditions of both air and hydrogen streams do not depend on the array spacing. To enable a fair comparison, it is important to keep the global equivalence ratio and the inflow properties of the fuel constant, as those are known to affect the mixing considerably.[6]

The injector spacing distance L_d is set to 0.01, 0.02, 0.04, and 0.057 m for cases C5d4, C5d2, C5, and C5d3 for which the fuel/air interface length per unit depth corresponds to 5, 3, 2, and 1.71, respectively. In the near field this parameter is the most representative of the mixing efficiency increase along x, as can be seen in Fig. 4, where the average mixing efficiency growth rate corresponds to 1.04, 0.68, 0.46, and 0.36 units per meter, where the ratios match the ratios of the fuel/air interface length per unit depth. This is a consequence of the limiting effect of the dilatational dissipation on turbulence growth at high turbulent Mach number. The high M_t is a consequence of the high shear stresses induced by the axial

vortices and by the fuel/air velocity difference. Without the addition of the compressibility correction term in the turbulence model, the correspondencebetween initial fuel/air interface length and mixing efficiency would not be present in the near field because of the sensitivity of the mixing layer growth to the axial vortices, which are reduced for small array spacing (Fig. 5). The important reduction in the mixing efficiency growth in the far field for cases C5d2 and C5d4 is attributed to the decrease in fuel/air contact surface area to the one exhibited by a two-dimensional planar configuration, with mixing only occurring at the top surface (Fig. 6).

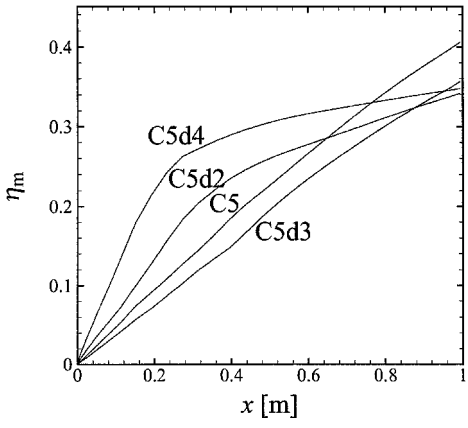

Fig. 4 Comparison between the mixing efficiency of cases C5 ($L_d = 0.04$), C5d2 ($L_d = 0.02$), C5d3 ($L_d = 0.057$), and C5d4 ($L_d = 0.01$).

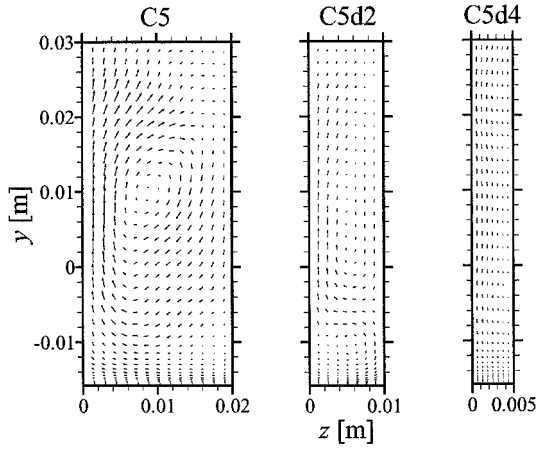

Fig. 5 Velocity vectors on a yz plane at $x = 0.32$ m for cases C5 ($L_d = 0.04$), C5d2 ($L_d = 0.02$), and C5d4 ($L_d = 0.01$); the arrow length is proportional to the magnitude of the cross-stream velocity vector, with the maximum length corresponding to 615 m/s.

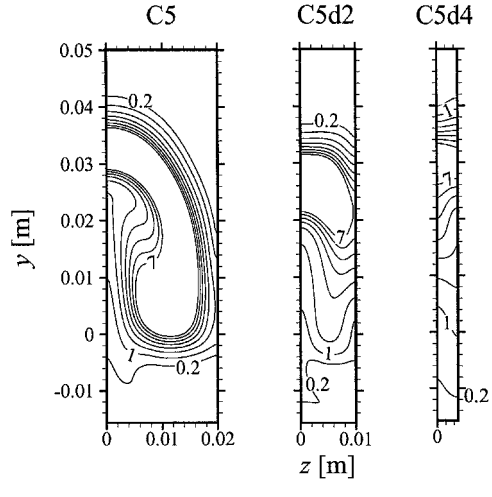

Fig. 6 Equivalence ratio contours at $x = 0.48$ m for cases C5d4 ($L_d = 0.01$ m), C5d2 ($L_d = 0.02$ m), and C5 ($L_d = 0.04$ m).

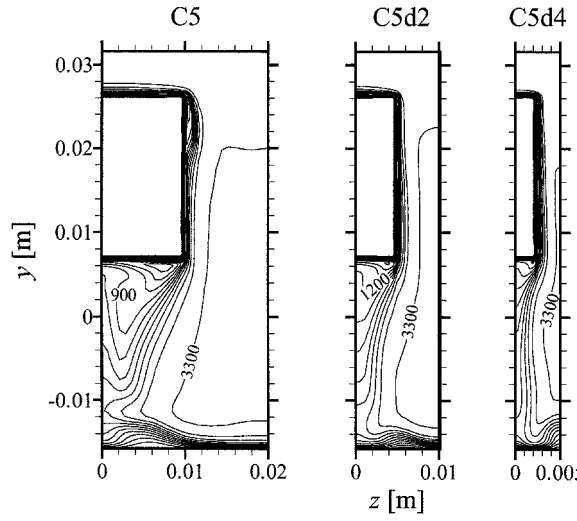

Fig. 7 Comparison between the x-velocity contours of cases C5 ($L_d = 0.04$), C5d2 ($L_d = 0.02$), and C5d4 ($L_d = 0.01$) at $x = 0$; the contours start at $u = 300$ m/s and end at $u = 5400$ m/s at increments of 300 m/s.

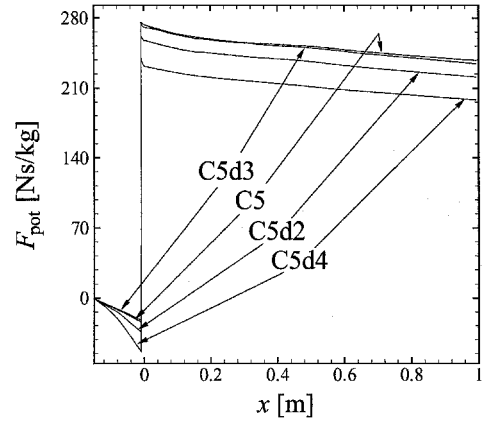

Fig. 8 Thrust potential of cases C5 ($L_d = 0.04$), C5d2 ($L_d = 0.02$), C5d3 ($L_d = 0.057$), and C5d4 ($L_d = 0.01$).

For an injector spacing less than the injector height (i.e., cases C5d2 and C5d4), the axial vortices are not strong enough to entrain enough incoming air below the fuel to prevent the hydrogen from entering the hot boundary layer, as shown by the equivalence ratio contours of Fig. 6. The reduction in strength of the axial vortices is attributed to the attenuated pressure difference between the flow above the injector and the flow on the injector side, which is a consequence of 1) the higher pressure between injectors induced by the increased area occupied by the boundary layer as seen in Fig. 7 and 2) the flattening of the shock above the injector.

Shown in Fig. 8, the thrust potential prior to injection decreases almost by a factor of two between cases C5d2 and C5d4 but does not vary significantly between cases C5 and C5d3. This is because of the thrust potential losses being boundary-layer dominated at a small array spacing, while being shock dominated at a high array spacing. Interestingly, this trend does not show up as much in the evaluation of the mass-flux-averaged stagnation pressure of Fig. 9. This is attributed to the high dependence of the thrust potential on 1) the stagnation temperature [as shown in Eq. (13)], which varies in the boundary layer, and 2) the backpressure of the engine, which is shown to vary considerably with the array spacing in Fig. 10.

Injection Angle

A parametric study of the injection angle is now given through cases C5c2, C5, and C5c, which use an injection angle of 4, 10, and 16 deg, respectively. At a higher angle the vortex originating at the top of the injector is stronger and induces greater magnitudes of the cross-stream velocity vector resulting in a more rapid motion of the fuel. The action of the top vortex on the fuel jet is shown through the equivalence ratio contours of Fig. 11. However, the

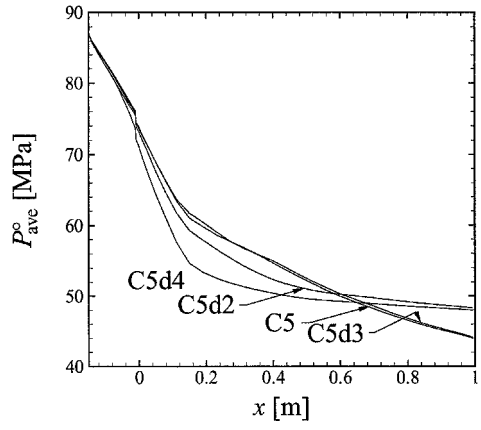

Fig. 9 Averaged stagnation pressure for cases C5 ($L_d = 0.04$), C5d2 ($L_d = 0.02$), C5d3 ($L_d = 0.057$), and C5d4 ($L_d = 0.01$).

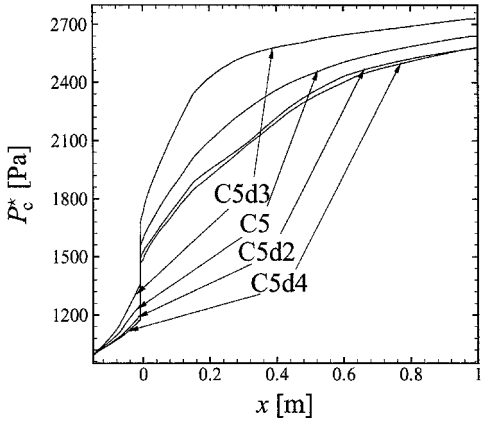

Fig. 10 Backpressure $P^{\star}_{c}$ (needed to determine P°) of cases C5 ($L_d = 0.04$), C5d2 ($L_d = 0.02$), C5d3 ($L_d = 0.057$), and C5d4 ($L_d = 0.01$).

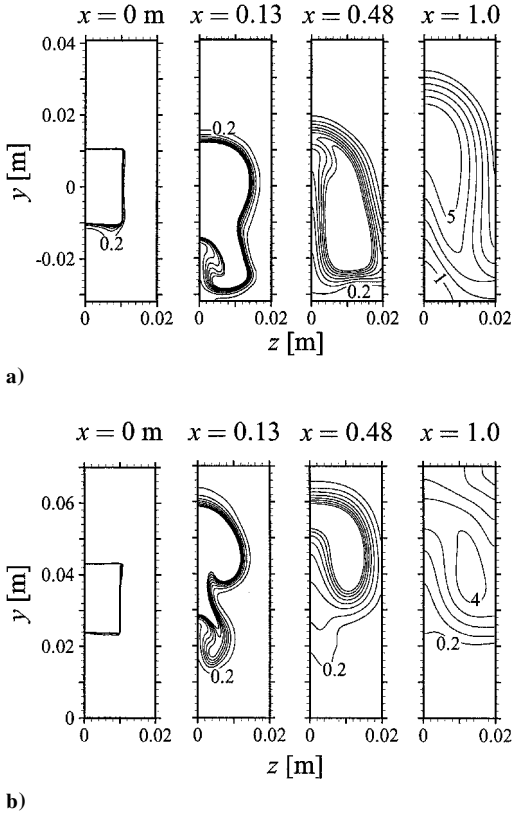

Fig. 11 Equivalence ratio contours of cases a) C5c2 ($\theta_c = 4$ deg) and b) C5c ($\theta_c = 16$ deg), with the contours located at $\phi = 0.2, 1, 2, \ldots, 7$.

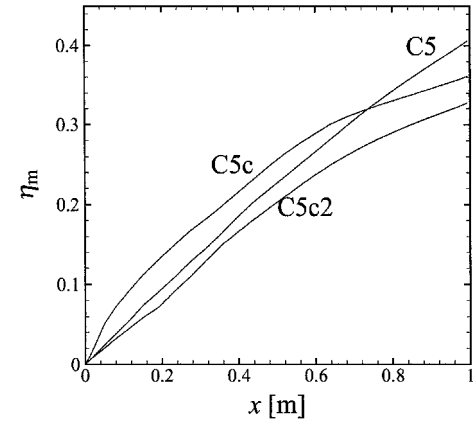

Fig. 12 Mixing efficiency of cases C5 ($\theta_c = 10$ deg), C5c ($\theta_c = 16$ deg), and C5c2 ($\theta_c = 4$ deg).

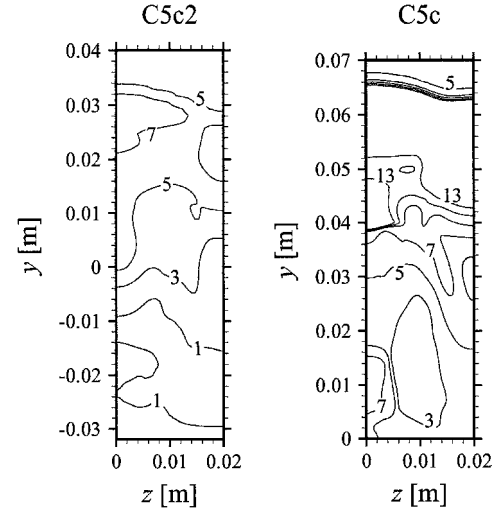

Fig. 13 Effective pressure contours at $x = 0.03$ m of cases C5c2 ($\theta_c = 4$ deg) and C5c ($\theta_c = 16$ deg); the contours start at $P^{\star} = 1$ kPa and end at $P^{\star} = 13$ kPa, at intervals of 2 kPa.

stronger vortex does not result directly into more mixing because it does not increase the contact surface between the hydrogen and the air. The fuel/air contact surface is even decreased in the near field compared to a low-angled injection by approximately 50%, a result of the hydrogen jet compression by the higher surrounding pressure. This seems to contradict the fact that the mixing efficiency growth in the near field is about two times higher for case C5c than for case C5c2 in Fig. 12. While decreasing the fuel/air contact surface, the higher pressure of case C5c (Fig. 13) is at the origin of the twofold difference in growth of the mixing efficiency. It is reminded that the mixing-layer growth is pressure independent, and because of a higher density of the flow at higher pressures the mixing layer spans through more mass flux of air and fuel, hence increasing the mixing efficiency growth.

The trend between the mixing efficiencies in the near field might not be all physical. At a high injection angle the fuel travels at a steep angle with the grid lines especially near the point of injection. This creates more numerical diffusion and results in more mixing. A grid-convergence study is performed using three different grid levels for a similar flowfield,[6] where it is indeed observed that the mixing efficiency is more sensitive to the grid in the near field.

The most striking difference in the equivalence ratio contours of Fig. 11, aside from the diminished streamwise vortex strength at lower θ_c, is the considerably shorter distance between the fuel and the bottom wall at a low injection angle. The direct cause of the less pronounced fuel penetration is the lower pressure of the air flowing under and between injectors at a lower injection angle. A lower pressure induces a lower density, which in turn induces a less pronounced mass flux of air flowing under the injector. This creates

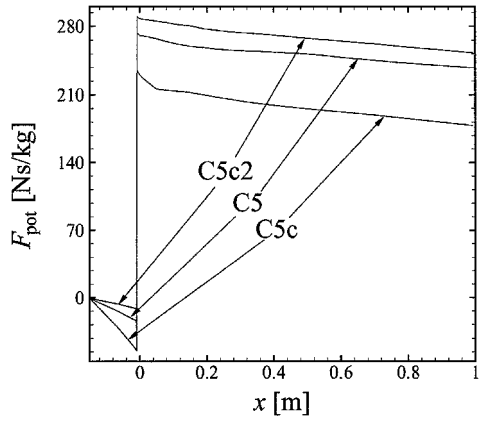

Fig. 14 Comparison between the thrust potential of cases C5 ($\theta_c = 10$ deg), C5c ($\theta_c = 16$ deg), and C5c2 ($\theta_c = 4$ deg).

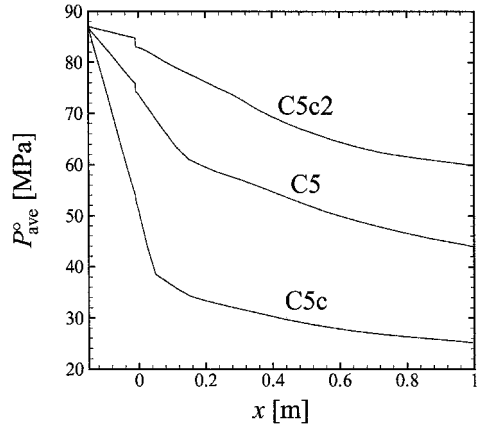

Fig. 15 Averaged stagnation pressure of cases C5 ($\theta_c = 10$ deg), C5c ($\theta_c = 16$ deg), and C5c2 ($\theta_c = 4$ deg).

the voidlike effect entraining the fuel to the wall that is observable in Fig. 11. For the $\theta_c = 4$-deg case, the fuel enters the boundary layer at $x = 0.1$ m, and is everywhere in the boundary layer for x greater than 0.8 m. It is emphasized that a combustible mixture in the hot boundary layer is undesirable as the fuel injection is intended to occur in the inlet of a high-speed flight vehicle, where no premature ignition is desired.

Figure 14 shows a fivefold increase in losses prior to injection between cases C5c ($\theta_c = 16$ deg) and C5c2 ($\theta_c = 4$ deg), with a similar thrust potential decrease observable in the far field for both cases. This is caused by the thrust potential loss originating mostly from the shock atop the injector, which exits the domain at $x \sim 0.10$ m (caused by the outflow boundary condition specified at the top of the domain). Should the top boundary condition be fixed to a wall instead of outflow, multiple shock reflections throughout the mixing region would probably maintain the fivefold difference in thrust potential throughout the flowfield. In this case the mass-averaged stagnation pressure (shown in Fig. 15) is a good indicator of the losses caused by the latter being strongly linked to the high strength shock over the injector, where the stagnation temperature is conserved. It has already been shown [see Eq. (13)] that at constant stagnation temperature the thrust potential depends only on the stagnation pressure and ambient pressure. For the low-angle injection case (case C5c2) the decrease in mixing efficiency far downstream for $x > 0.65$ m (as shown in Fig. 12) is as a result of the reduced fuel/air contact surface caused by a rapid erosion of the air pocket between the fuel and the wall. On the other hand, the decrease in mixing for case C5c in the far field is believed to be related to a numerical accuracy issue: as the fuel/air mixture exits the domain through the top boundary at approximately $x = 0.6$ m, it does not contribute anymore to the mixing efficiency growth, which progressively diminishes.

Incoming Boundary Layer

One might expect a higher amount of turbulence at injection generated through a long flat plate as in case C5f (with $L_f = 0.5$ m in Fig. 1) to increase the turbulence present through the mixing layer. An increased amount of turbulence could then contribute to the mixing-layer spread and hence augment the mixing efficiency. This trend is observed by the authors for a ramp injector where the turbulent Mach number is low (case shown in Waitz et al.[5]) and where the addition of an incoming flat plate prior to the injector increases the mixing efficiency. The turbulence induced through a velocity difference between fuel and air and through the cross-stream shear stresses created by the axial vortices is nonetheless very weak for the Waitz case, and compressibility effects play a minor role. For the C5 case shown herein the compressibility effects limit the mixing-layer

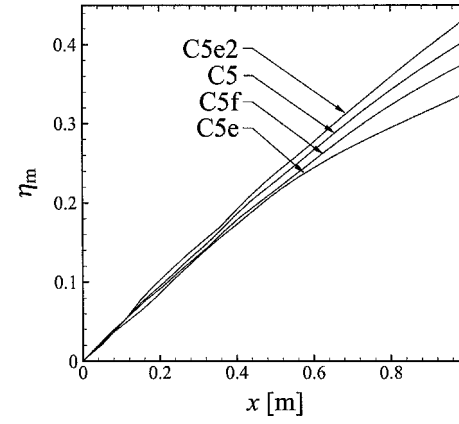

Fig. 16 Mixing efficiency of cases C5e2 (−3.5-deg sweeping angle), C5, C5f (with a 50-cm-long incoming flat plate prior to injection), and C5e (3.5-deg sweeping angle).

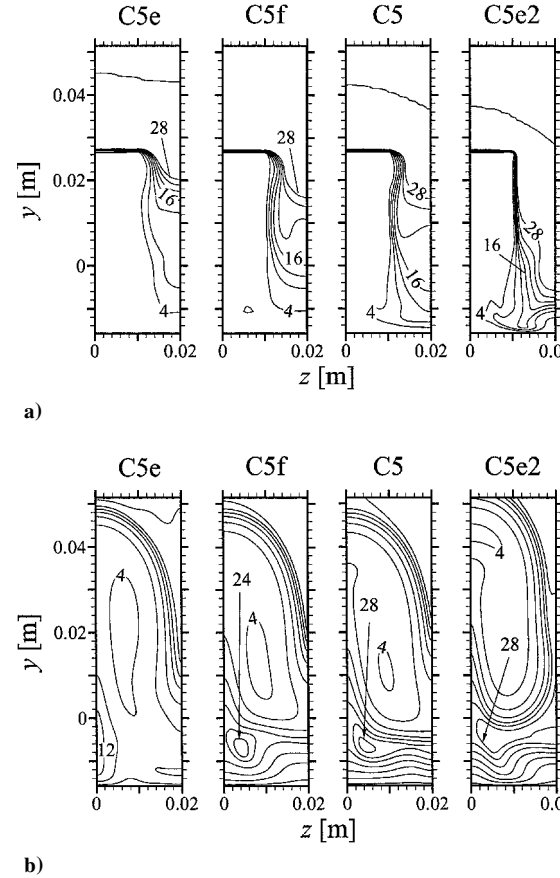

Fig. 17 Contours of the mass flux of oxygen in the x direction ($\rho u c_{O_2}$) at a) $x = 0$ m and b) $x = 0.7$ m for cases C5, C5f, C5e, and C5e2; the contour lines start at 4 kg/m^{2}s until 28 kg/m^{2}s at intervals of 4 kg/m^{2}s.

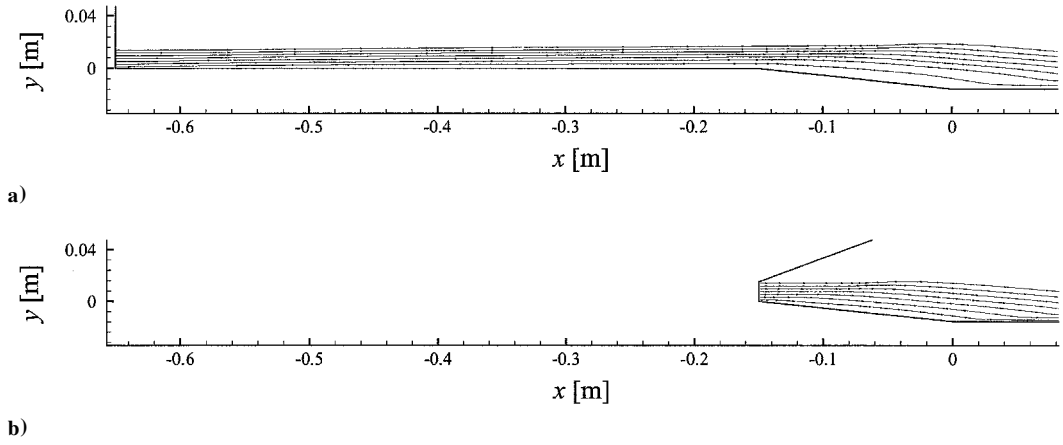

Fig. 18 Comparison of the vector traces (created from the velocity components along x and y only) between cases a) C5f and b) C5 in the symmetry plane in between the injectors. The vector traces originate on the inflow plane at $y = 0.001, 0.003, \ldots, 0.011, 0.013$ m for both cases.

growth, and the addition of incoming turbulence does not help the spreading rate. Figure 16 shows even a decrease in mixing efficiency when a flat plate is concatenated to the cantilevered injector domain. The decrease is not too pronounced and has a higher effect far downstream at $x > 0.5$ m, which is attributed to a decrease of oxygen mass flow under the fuel (see Fig. 17). For $x > 0.7$ m this affects the mixing efficiency growth by reducing the contact surface area between fuel and air, especially far downstream, where the cushion is almost all eroded. A comparison of the streamlines between cases C5 and C5f in Fig. 18 reveals that the reduced amount of oxygen between the fuel and the wall is caused by the lifting effect on the incoming air by the boundary layer.

Sweeping Angle

The use of a sweeping angle has been observed by others[10–13] to result into stronger axial vortices and better overall mixing characteristics. However, for the cantilevered ramp injector shown herein at a convective Mach number of 1.5 the opposite trend is observed: as the sweeping angle is increased to 3.5 deg, the mixing efficiency decreases by 17%, as shown in Fig. 16. The use of a swept configuration is not beneficial to the mixing efficiency at a high convective Mach number because of the growth of the mixing layer already being limited by the dilatational dissipation term. Although it is true that the addition of stronger axial vortices results in stronger cross-stream shear stresses, this does not translate into more mixing as the mixing-layer growth is limited by the compressibility effects. Further, it can be seen in Fig. 17 that the use of a sweeping configuration decreases significantly the amount of oxygen flowing on the sides of the cantilevered injector. This is a direct consequence of the swept configuration creating a stronger and flatter shock wave above the injector, which deflects the incoming air upwards and hence diminishes the oxygen mass flux on the sides of the injector. This results in a reduction of the air cushion under the fuel later downstream. It is emphasized that the reduction in airflow rate under and between injectors is detrimental for two reasons: 1) it reduces the air cushion between the fuel and the hot boundary layer, which increases the chance of premature ignition (an undesirable feature, as this injection study simulates fuel injection in the inlet of a detonation-wave ramjet); and 2) far downstream, it eventually reduces the contact surface area between fuel and air, as the mixing layer "runs out" of air mass flow near the wall. The second reason is the cause of the reduction of 17% in the mixing efficiency between cases C5 and C5e observable in Fig. 16. Interestingly, the use of a negative sweeping angle results in a more pronounced fuel penetration as attested by the equivalence ratio contours of Fig. 19. This is because the sides of the injector are acting as compression surfaces, hence entraining a greater amount of oxygen mass flux between the ramps at the point of injection (see Fig. 17a). The higher amount of oxygen at the base of the ramps, entrained under the fuel by the axial vortices, increases the size of the air buffer under the fuel later downstream. This results in a greater fuel/air contact surface, and

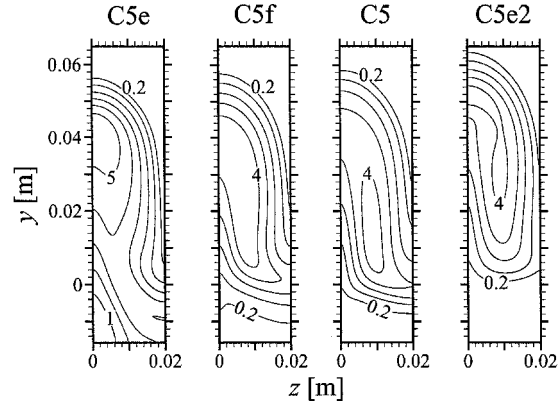

Fig. 19 Contours of the equivalence ratio at $x = 1.0$ m for cases C5, C5f (50-cm-long flat plate), C5e (3.5-deg sweeping angle), and C5e2 (−3.5-deg sweeping angle); the contour lines are at $\phi = 0.2, 1, 2, \ldots, 5$.

consequently, the observed increase of 28% of the mixing efficiency between case C5e ($\psi = 3.5$ deg) and case C5e2 ($\psi = -3.5$ deg).

Conclusions

A parametric study of the variation of the injector array spacing shows that the mixing efficiency at the domain exit is maximal for an array spacing equal to the height of the injector. Reducing the spacing diminishes considerably the axial vortices strength but increases the contact surface between fuel and air at the point of injection. The rate of growth of the mixing efficiency in the nearfield is observed to be directly related to the fuel/air contact surface at injection. The decrease in the axial vortices strength at a small array spacing prevents enough air from being entrained under the fuel jet, resulting in a combustible mixture present in the boundary layer. Because of the higher shock strength present above the injector, a high angle of injection translates into significantly more losses: injecting the fuel at 16 deg results in a twofold increase in the thrust potential losses compared to injection at 4 deg with an associated increase in mixing efficiency of 9%.

If the cantilevered ramp injector is destined to be used in the inlet of a shcramjet where premature burning should be avoided, it must be ensured that no fuel enters the hot hypersonic boundary layer. For some of the test cases obtained, it is found that hydrogen enters the boundary layer because of the reduction of the air cushion between the fuel jet and the wall. The reduction in the air cushion is caused by weakened axial vortices and/or by a lower air mass flux flowing under the fuel at the point of injection. It is observed that an air cushion between the wall and the hydrogen is sufficiently thick to prevent fuel in the boundary layer when 1) the fuel is injected at an angle of ~10 deg or more, 2) an array spacing of at least the height of the injector is used, and 3) a swept ramp configuration is

avoided. An incoming boundary layer with a thickness of 15% the injector height is noticed not to diminish significantly the air cushion between the fuel and the wall, whereas a sweeping angle of −3.5 deg is observed to result into significantly better fuel penetration.

The mass-flux-averaged stagnation pressure is shown to be deficient in assessing the losses because of the strong dependency of the thrust potential on the backpressure of the engine and on variations of the flow stagnation temperature. To correctly assess the impact of the backpressure on the losses, the thrust potential is here determined by reversibly expanding the flow to a fixed area and by imposing the same pressure on all streamlines. The addition in thrust potential by the fuel momentum is seen to be greater than the losses incurred by irreversible phenomena for all cases studied herein.

Acknowledgment

This work has been supported by the Natural Sciences and Engineering Research Council.

References

[1]Dudebout, R., Sislian, J. P., and Oppitz, R., "Numerical Simulation of Hypersonic Shock-Induced Combustion Ramjets," *Journal of Propulsion and Power*, Vol. 14, No. 6, 1998, pp. 869–879.

[2]Papamoschou, D., and Roshko, A., "The Compressible Turbulent Shear Layer: an Experimental Study," *Journal of Fluid Mechanics*, Vol. 197, 1988, pp. 453–477.

[3]Papamoschou, D., "Thrust Loss due to Supersonic Mixing," *Journal of Propulsion and Power*, Vol. 10, No. 6, 1994, pp. 804–809.

[4]Marble, F., Zukoski, E., Jacobs, J., Hendricks, G., and Waitz, I., "Shock Enhancement and Control of Hypersonic Mixing and Combustion," AIAA Paper 90-1981, July 1990.

[5]Waitz, I. A., Marble, F. E., and Zukoski, E. E., "Investigation of a Contoured Wall Injector for Hypervelocity Mixing Augmentation," *AIAA Journal*, Vol. 31, No. 6, 1993, pp. 1014–1021.

[6]Parent, B., Sislian, J. P., and Schumacher, J., "Numerical Investigation of the Turbulent Mixing Performance of a Cantilevered Ramp Injector," *AIAA Journal*, Vol. 40, No. 8, 2002, pp. 1559–1566.

[7]Sislian, J. P., and Schumacher, J., "A Comparative Study of Hypersonic Fuel/Air Mixing Enhancement by Ramp and Cantilevered Ramp Injectors," AIAA Paper 99-4873, Nov. 1999.

[8]Parent, B., and Sislian, J. P., "Turbulent Hypervelocity Fuel/Air Mixing by Cantilevered Ramp Injectors," AIAA Paper 2001-1888, April 2001.

[9]Waitz, I., Marble, F., and Zukoski, E., "A Systematic Experimental and Computational Investigation of a Class of Contoured Wall Fuel Injectors," AIAA Paper 92-0625, Jan. 1992.

[10]Riggins, D. W., and Vitt, P. H., "Vortex Generation and Mixing in Three-Dimensional Supersonic Combustors," *Journal of Propulsion and Power*, Vol. 11, No. 3, 1995, pp. 419–426.

[11]Riggins, D. W., McClinton, C. R., Rogers, R. C., and Bittner, R. D., "A Comparative Study of Scramjet Injection Strategies for High Mach Number Flows," AIAA Paper 92-3287, July 1992.

[12]Donohue, J. M., McDaniel, J. C., and Haj-Hariri, H., "Experimental and Numerical Study of Swept Ramp Injection into a Supersonic Flowfield," *AIAA Journal*, Vol. 32, No. 9, 1994, pp. 1860–1867.

[13]Drummond, J. P., "Enhancement of Mixing and Reaction in High-Speed Combustor Flowfields," International Symposium on Air Breathing Engines, Paper 97-7024, May 1997.

[14]Parent, B., and Sislian, J. P., "The Use of Domain Decomposition in Accelerating the Convergence of Quasihyperbolic Systems," *Journal of Computational Physics*, Vol. 179, No. 1, 2002, pp. 140–169.

[15]Wilcox, D. C., "Reassessment of the Scale Determining Equation for Advanced Turbulence Models," *AIAA Journal*, Vol. 26, No. 11, 1988, pp. 1299–1310.

[16]Wilcox, D. C., "Dilatation-Dissipation Corrections for Advanced Turbulence Models," *AIAA Journal*, Vol. 30, No. 11, 1992, pp. 2639–2646.

[17]McBride, B. J., and Reno, M. A., "Coefficients for Calculating Thermodynamic and Transport Properties of Individual Species," NASA TM 4513, 1993.

[18]Yee, H. C., Klopfer, G. H., and Montagné, J.-L., "High-Resolution Shock-Capturing Schemes for Inviscid and Viscous Hypersonic Flows," *Journal of Computational Physics*, Vol. 88, No. 1, 1990, pp. 31–61.

[19]Laney, C. B., *Computational Gasdynamics*, Cambridge Univ. Press, New York, 1998, p. 68.

[20]Chang, C.-L., and Merkle, C. L., "The Relation Between Flux Vector Splitting and Parabolized Schemes," *Journal of Computational Physics*, Vol. 80, No. 2, 1989, pp. 344–361.

[21]Riggins, D. W., McClinton, C. R., and Vitt, P. H., "Thrust Losses in Hypersonic Engines Part 1: Methodology," *Journal of Propulsion and Power*, Vol. 13, No. 2, 1997, pp. 281–287.

[22]Pratt, D. T., and Heiser, W. H., *Hypersonic Airbreathing Propulsion*, AIAA Education Series, AIAA, Washington, DC, 1994, p. 387.

J. P. Gore
Associate Editor